The nested morphology of disk winds from young stars revealed by JWST/NIRSpec observations

Ilaria Pascucci[1*], Tracy L. Beck[2], Sylvie Cabrit[3], Naman S. Bajaj[1], Suzan Edwards[4], Fabien Louvet[5], Joan Najita[6], Bennett N. Skinner[1,7], Uma Gorti[8,9], Colette Salyk[10], Sean D. Brittain[11], Sebastiaan Krijt[12], James Muzerolle Page[2], Maxime Ruaud[8], Kamber Schwarz[13], Dmitry Semenov[13,14], Gaspard Duchene[5,15], Marion Villenave[16]

[1*]Lunar and Planetary Laboratory, The University of Arizona, 1629 E. University Blvd., Tucson, 85721, Arizona, USA.
[2]Instruments Division, Space Telescope Science Institute, 3700 San Martin Drive, Baltimore, 21218, Maryland, USA.
[3]Observatoire de Paris, LERMA, CNRS, Paris, 75014, France.
[4]Five College Astronomy Department, Smith College, Northampton, 01063, MA, USA.
[5]University of Grenoble Alpes, CNRS, IPAG, Grenoble, 38000, France.
[6]NOIRLab, NSF, 950 N Cherry Avenue, Tucson, 85719, Arizona, USA.
[7]Department of Physics and Astronomy, McMaster University, Hamilton, L8S 4M1, Ontario, Canada.
[8]Ames Research Center, NASA, Moffett Field, 94035, CA, USA.
[9]Carl Sagan Center, SETI Institute, Mountain View, 94035, CA, USA.
[10]Department of Physics and Astronomy, Vassar College, 124 Raymond Ave, Poughkeepsie, 12604, NY, USA.
[11]Department of Physics and Astronomy, Clemson University, Clemson, 29634, SC, USA.
[12]Department of Physics and Astronomy, University of Exeter, Stocker Road, Exeter, EX4 4QL, UK.
[13]Max-Planck-Institut für Astronomie, Königstuhl 17, Heidelberg, D-69117, Germany.
[14]Department of Chemistry, Ludwig-Maximilians-Universität, Butenandtstr. 5-13, München, D-81377, NY, Germany.

[15]Department of Astronomy, University of California, Berkeley, 94720, CA, USA.
[16]Dipartimento di Fisica, Università degli Studi di Milano, Via Giovanni Celoria 16, Milano, 20133, Italy.

*Corresponding author(s). E-mail(s): pascucci@arizona.edu;
Contributing authors: tbeck@stsci.edu; sylvie.cabrit@obspm.fr; namanbajaj@arizona.edu; sedwards@smith.edu; fabien.louvet@univ-grenoble-alpes.fr; joan.najita@noirlab.edu; skinnb1@mcmaster.ca; uma.gorti-1@nasa.gov; cosalyk@vassar.edu; sbritt@clemson.edu; s.krijt@exeter.ac.uk; muzerol@stsci.edu; maxime.ruaud@nasa.gov; schwarz@mpia.de; semenov@mpia.de; gaspard.duchene@univ-grenoble-alpes.fr; marion.villenave@unimi.it;

Abstract

Radially extended disk winds could be the key to unlocking how protoplanetary disks accrete and how planets form and migrate. A distinctive characteristic is their nested morphology of velocity and chemistry. Here we report JWST/NIRSpec spectro-imaging of four young stars with edge-on disks, **three of which have already dispersed their natal envelopes**. In each source, a fast collimated jet traced by [Fe II] is nested inside a hollow cavity within wider lower-velocity H_2. **In one case a hollow structure is also seen in CO rovibrational (v=1-0) emission but with a wider opening angle than the H_2, and both of those are** nested inside an ALMA CO **(J=2-1)** cone with an even wider opening angle. This nested morphology **even in sources with no envelope** strongly supports theoretical predictions for wind-driven accretion and underscores the need for theoretical work to assess the role of winds in the formation and evolution of planetary systems.

Keywords: Protoplanetary Disks, Jets, Disk Winds, Planet Formation

1 Introduction

The assembly of stars and their planetary systems proceeds through an accretion disk where magneto-rotational instability (MRI, Balbus and Hawley 1) was long favored to transport angular momentum outward, aiding inward accretion. Recent simulations, incorporating disk microphysics, challenge this view, showing MRI is suppressed in most of the planet-forming region ($\sim 1-20$ au). Instead, radially extended magnetohydrodynamic (MHD) disk winds – outflowing gas from a few scale heights above the disk midplane launched by magnetic and thermal pressures – emerge as a viable mechanism for angular momentum removal and for enabling accretion [e.g., 2, and

references therein]. This new wind-driven accretion scenario greatly impacts the evolution of the disk surface density [e.g., 3], affecting the inward drift of solids [e.g., 4] and where planets may form and migrate to [e.g., 5].Consequently, observations that can confirm the presence of these winds are crucial.

A unique feature of radially extended MHD winds is that flows are launched over a broad range of disk radii, hence outflow velocities, from near the gas co-rotation radius ($\sim$ 0.1 au) across much of the planet-forming region [e.g., 6]. This contrasts with X-winds, where stellar field lines couple **narrowly** to the disk at the co-rotation radius and launch fast ($\sim$ 150 km/s) MHD winds that spread widely [e.g., 7], and photoevaporative winds, which only develop where disk gas has enough thermal energy to escape the stellar gravitational field, beyond $\sim$ 1 au and with speeds $\leq$ 10 km/s [e.g., 8]. Another distinctive characteristic of **radially extended** MHD winds is their nested morphology of velocity and chemistry throughout all stages of star-disk evolution: a fast $\sim$ 100 km/s jet, formed by the recollimation of the inner wind, lies inside atomic and molecular gas moving at sequentially lower velocities [e.g., 9]. X-winds can also collimate a jet [e.g., 10]. However, lower-velocity flows arise solely from material entrained by the fast wind, which sweeps up gas near the disk surface [11] and, when an infalling envelope is present, also gathers envelope material near the disk's outer edge [e.g., 12]. Conversely, in the photoevaporative scenario, the absence of recollimation means fast jets are not produced, and the wind's opening angle remains close to that at launch [e.g., 13].

Current kinematic data on young ($\sim$ 0.1 $-$ 10 Myr) stars with a mass greater than that of the infalling envelope – Class I and II sources [e.g., 14] – hint at the presence of radially extended MHD winds. Spatially unresolved spectra of optical forbidden emission like [O I] and near-infrared emission of H_2 can show, in addition to a high velocity component ($\sim 50-300$ km/s) tracing the base of a jet, a second lower velocity component with broad line widths interpreted as originating over disk radii $\sim 0.5-5$ au [e.g., 15]. A handful of spatially resolved outflows point to velocities which decrease outwards, with the narrow fast jet **along the axis of** a wider-angle lower velocity flow [e.g., 16, and references therein]. However, the limited number of spatially resolved flows **especially in sources that have dispersed their natal envelopes** [e.g., 17–19] has thus far hindered a detailed mapping of the wind morphology across chemical species, leaving the predicted nested structure by radially extended MHD winds uncertain.

2 Results

We used the near-infrared spectrograph (NIRSpec) on the James Webb Space Telescope (JWST, Böker et al. 24) to acquire deep spectro-imaging of four edge-on disks with known jets [e.g., 21]. All sources belong to the nearby ($\sim$ 140 pc) and young ($\sim 1-2$ Myr) Taurus star-forming region [e.g., 25], see Table 1 for properties relevant to this study. While infrared spectral indices are often used to assign Classes to young stellar systems as proxies for their evolutionary stage [e.g., 26], this method is unreliable for edge-on disks [27]. Comparing the ALMA millimeter disk fluxes (Table 1 and

Table 1 Literature source properties relevant to this study.

Source	RA(J2000) (h m s)	Dec(J2000) (° ′ ″)	M_* ($M_\odot$)	F_{mm} (mJy)	PA_{mm} (°)	i_{mm} (°)	R_{mm} (au)	R_{ir} (au)	Ref.
FS Tau B	04 22 00.7	+26 57 32.5	0.7	341	145	74	144	161	1,2
HH 30	04 31 37.5	+18 12 24.5	0.5	55	121	> 85	130	217	2,3
IRAS 04302	04 33 16.5	+22 53 20.4	1.3-1.7	268	175	> 84	220		1,2
Tau 042021	04 20 21.4	+28 13 49.2	0.4	124	-16	> 85	287	350	2,4

Notes. M_* is inferred from the disk gas Keplerian rotation, observed via well-resolved mm-wavelength spectro-imaging of molecular lines. F_{mm}, PA_{mm}, i_{mm}, R_{mm} are the flux density, position angle, inclination, and disk radius from spatially resolved ALMA Band7 (0.89 mm) continuum images, which trace millimeter-size grains. R_{ir} is the disk radius from optical/near-infrared scattered light images, thus probing small sub-micron grains well coupled with the gas.
References. (1) Simon et al. [20]; (2) Villenave et al. [21]; (3) Louvet et al. [22]; (4) Duchene et al. [23]

Villenave et al. 21) with single-dish fluxes [28–31] reveals that only IRAS 04302 is surrounded by a significant envelope. The other sources' fluxes are primarily from disk emission pointing to a more evolved evolutionary stage **with no significant infalling envelope** that aligns with the Class II category.

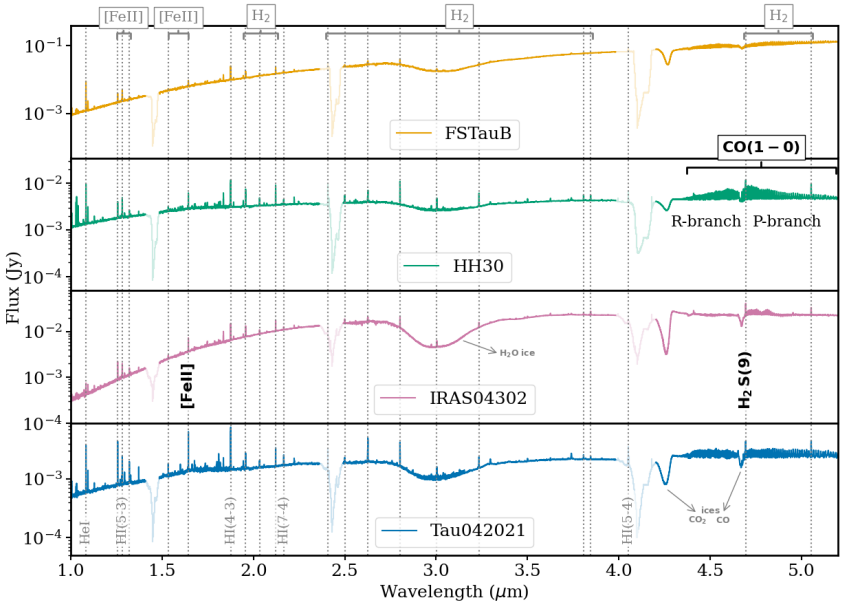

Fig. 1 Spectra integrated over the NIRSpec IFU **with semi-transparent regions indicating the minimum and maximum wavelength cutoff of the detectors' gaps. The H_2O, CO_2, and CO ice bands are identified with gray arrows.** A few of the strongest **emission** lines are marked with gray dotted lines. All of these lines are spatially extended. The transitions analyzed in this study are highlighted in boldface.

NIRSpec IFU covers a field-of-view of $\sim 3'' \times 3''$ with a pixel scale of $0.1''$ and, with our use of the three high-resolution gratings, delivers $0.95 - 5.27\,\mu$m spectra at each pixel with a velocity sampling of ~ 40 km/s (see Sect. 4 for details on the observations and data reduction). Multiple [Fe II], H, and H_2 lines are detected in the integrated spectra along with the P- and R-branches of the CO (v=1-0) ro-vibrational transition at $\sim 4.7\,\mu$m (see Figure 1 highlighting some of the detected lines). Here, we focus on the brightest [Fe II] line at $1.644\,\mu$m, a known jet tracer [e.g., 32], the H_2 0-0 S(9) line at $4.695\,\mu$m, and the CO (v=1-0) band. We selected the H_2 S(9) line, the brightest long-wavelength transition in our sample, due to significantly lower scattering from the disk surface relative to shorter wavelengths H_2 lines, like the often-studied $2.12\,\mu$m 1-0 S(1) line. Its integrated flux is at most half that of the S(1) line (Table 2 and Sect. 4), thereby combining the advantages of tracing the H_2 morphology closer to the disk with considerable relative brightness. The similarity of the [Fe II] fluxes in our sample (Table 2) hints at similar jet mass loss rates. Considering the estimate for HH 30 of $2 \times 10^{-9}\,M_\odot$/yr [33] and factoring in the typical jet/accretion ratio of approximately 0.1 [34], it is likely that our sources are accreting at rates exceeding $10^{-8}\,M_\odot$/yr. This inference is supported by the sole literature mass accretion rate available for our sample, the one from FS Tau B which is $\sim 1.5 \times 10^{-7}\,M_\odot$/yr [35].

The sub-panels of Figure 2 show PSF-deconvolved, continuum-subtracted line maps of the $1.644\,\mu$m [Fe II] line, the H_2 0-0 S(9) line, along with the sum of the CO P-branch lines between $\sim 4.7 - 4.9\,\mu$m (see Sect. 4 for details). The continuum emission below the H_2 S(9) line, which traces scattered light by small grains at the disk surface, is also displayed in one of the sub-panels. The main panels show three-color composite images combining the [Fe II] and H_2 lines with the continuum emission. Additionally, integrated CO P-branch contours are overlaid in gray. [Fe II] traces the narrow jet emission and we have verified that its position angle is perpendicular to the ALMA millimeter disk (Tables 1 and 2). We have also generated H_2 maps for the **1-0 S(1) at** $2.12\,\mu$m and the **0-0 S(8) at** $5.05\,\mu$m lines and found similar morphologies to the H_2 0-0 S(9) line which is thus representative for the molecular hydrogen gas. In addition, we created velocity centroid maps for the [Fe II] and H_2 lines and found that the NIRSpec resolution can discern small shifts between the blue and red lobe of the [Fe II] jets (see Sect. 4). Images in Figure 2 were then rotated to align the blueshifted jet emission vertically at the top of each panel. The H_2 maps show no **resolved** velocity structure, as expected if molecular gas moves at lower speeds than the jet.

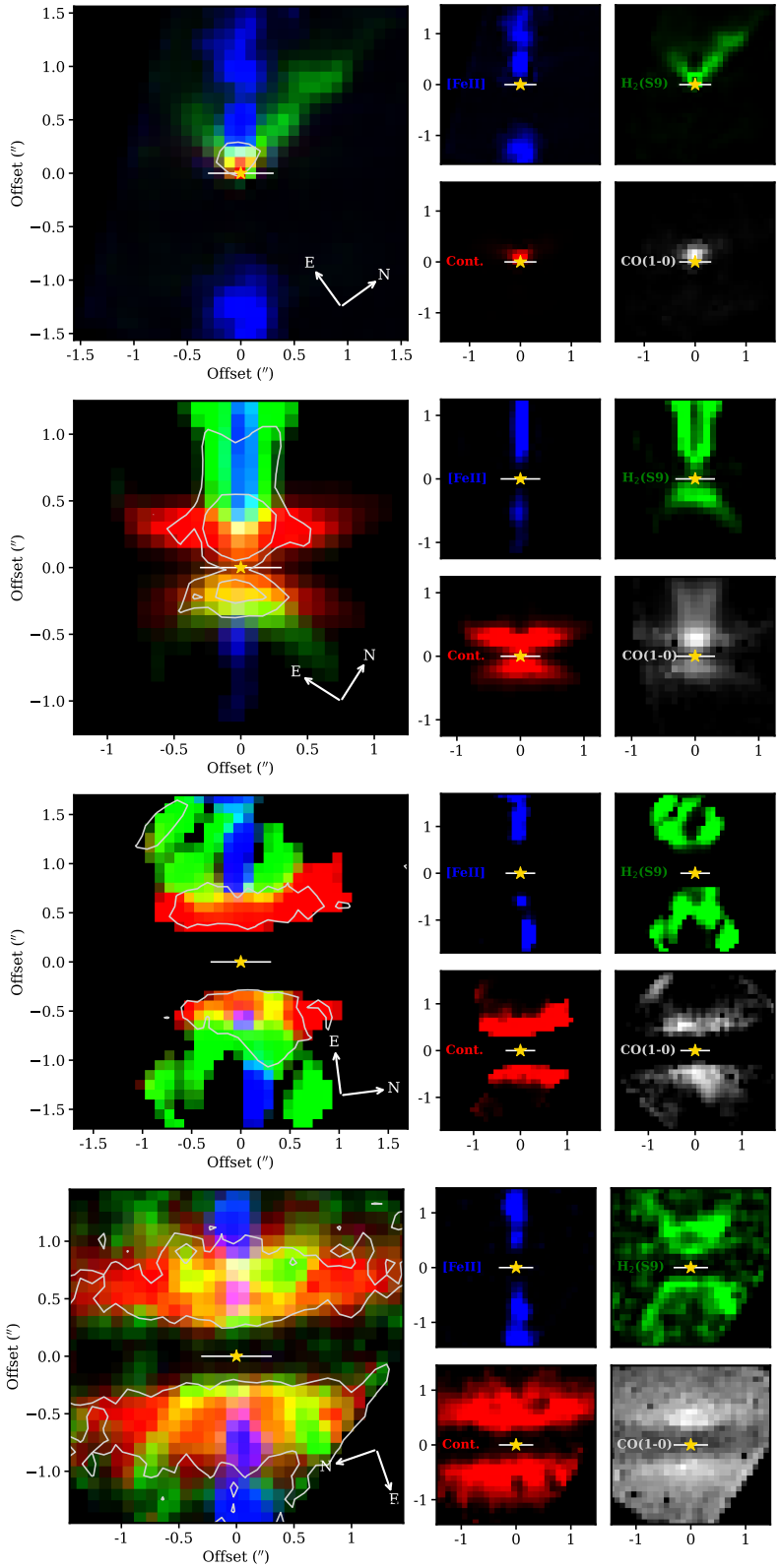

Fig. 2 Composite NIRSpec images: [Fe II] emission at 1.644 μm (blue) – H_2 0-0 S(9) emission at 4.695 μm (green) – continuum emission at the H_2 line (red). CO emission from $\sim$ 4.7 – 4.9 μm is shown in the right bottom sub-panel in gray – the 50% of the peak emission contour (and for HH 30 also the 30%) is shown in gray in the composite image. In every instance, the collimated jet traced in [Fe II] is nestled inside the wider H_2 emission and, in the case of HH 30, also the CO (v=1-0) emission.

In every source, the narrow [Fe II] jet is nested within wider H_2 emission, which is always more vertically extended than the continuum emission at the same wavelength. While the overall **[Fe II]/H_2 morphology, with a narrow atomic jet along the axis of a wider H_2 cone,** has been seen in a few other sources [e.g., 17, 36, 37] revealed for the first time is the **presence of a** central cavity **in the H_2 cone. Emission in a cone with a hollow center, in the absence of ambient material, is** expected if H_2 traces **material lifted from the disk, i.e. a disk wind,** emerging from a larger **radial distance** than the jet [e.g., 9]. Extended CO ro-vibrational emission is detected in three sources. Uniquely in HH 30, this emission mirrors the H_2 conical morphology, albeit less vertically extended, with a central cavity surrounding the jet. **This marks the first resolved mapping of a wind-like structure in the CO (v=1-0) band (see e.g., Jensen et al. 38 and references therein for indications of winds in this tracer through spectro-astrometry).**

Significant brightness asymmetry relative to the disk plane is seen in the jet and wind features for two of our sources: FS Tau B and HH 30. In both cases the more prominent emission is on the side of the disk where the jet is blueshifted. While this asymmetry has been known for their jets [39, 40], it is now seen in the winds as well. This discovery is particularly noteworthy for FS Tau B, marking the first such observation in its wind. For HH 30, our finding corroborates the asymmetry previously noted in the millimeter CO **(J=2-1)** wind emission [22].

For each source, we trace the [Fe II] jet and H_2 wind emission to quantify their semi-opening angles (θ_j and θ_w) and estimate the radii where the wind intersects the disk plane (geometric radii, R_{geo}), see Sect. 4 for details and Table 2 for the results. Jet semi-opening angles vary **between** $\sim 2.5° - 17°$, consistently smaller than their corresponding wind semi-opening angles which range **from** $\sim 13°$ **to** $50°$. HH 30 stands out as having the most collimated jet and narrowest wind among our sources (Figure 3), although similarly narrow jets have been reported in other Class II sources [e.g., 41]. The wind semi-opening angle we estimate for Tau 042021 is the same as that recently reported in [42] using a lower spatial resolution H_2 S(2) map obtained with JWST/MIRI. Our PSF-deconvolved images enable measuring the semi-opening angle of its jet, which was unresolved with MIRI. In addition, they allow placing stringent constraints on the intersection points of the H_2 cones with the disk plane. Specifically, we determine these intersections occur at $R_{geo} < 0.1''$ **(Table 2, 14 au at the average distance of Taurus), well inside the disk outer radii of** $\sim 150 - 350$ **au**. If these cones trace MHD winds, the decreasing wind opening angle with height due to magnetic recollimation [e.g., 43] implies that each R_{geo} defines an upper boundary for the actual wind-launching radius.

Table 2 Inferred jet and wind properties. The [Fe II] and H_2 lines we have selected are among the most prominent tracers of jets and winds, respectively.

Source	Jet: [Fe II] 1.644 μm			Wind: H_2 0-0 S(9) 4.695 μm		
	Flux	PA	θ_j	Flux	θ_w	R_{geo}
	(erg/s/cm^2)	(°)	(°)	(erg/s/cm^2)	(°)	($''$)
FS Tau B	4.1×10^{-15}	55±3	**16.8±5.1**	3.5×10^{-15}	**41.2±15.8**	**-0.05±0.15**
					50.3±4.5	**-0.03±0.05**
HH 30	2.0×10^{-15}	32±2	**2.6±1.1**	1.5×10^{-15}	**14.1±1.1**	-0.04±0.01
					12.8±1.1	0.05±**0.01**
IRAS 04302	3.0×10^{-15}	87±2	**7.5±1.7**	$\mathbf{4.0}\times10^{-15}$	**38.7±7.7**	**-0.04±0.09**
					27.8±3.5	**0.04±0.03**
Tau 042021	$\mathbf{3.2}\times10^{-15}$	72±2	**5.3±2.0**	4.5×10^{-16}	**38.5±8.9**	**-0.02±0.08**
					37.6±5.3	**0.04±0.05**

Notes. For each source we list the jet's semi-opening angle (θ_j) and the wind's semi-opening angle (θ_w) and **extrapolated radius at z=0** (R_{geo}) for both lobes of the blue-shifted emission. FS Tau B's disk is less inclined than the others, hence the disk plane and R_{geo} are less well determined (see Sect. 4). **The uncertainty in the integrated line fluxes is dominated by the 10% absolute photometric accuracy of the NIRSpec spectra (Böker et al. 24 and Sect. 4).**

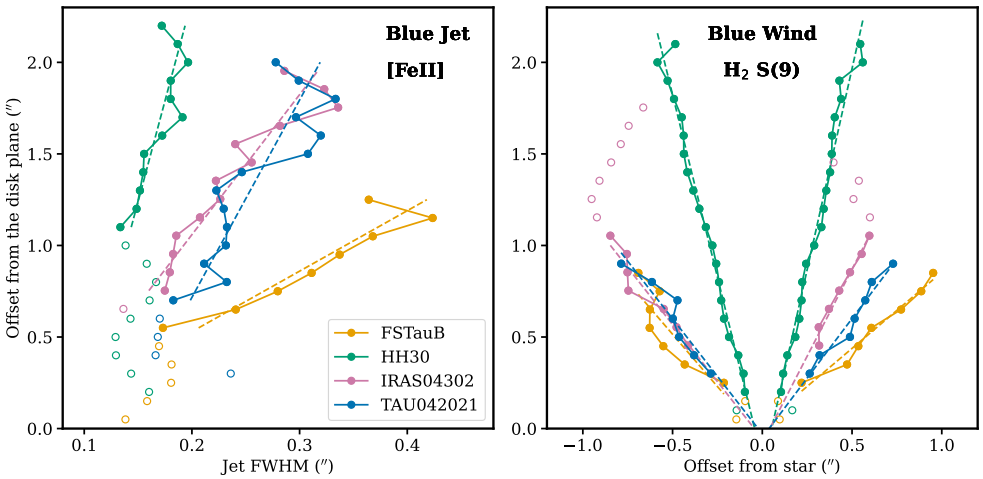

Fig. 3 Left panel: FWHM of the jet's blueshifted component as a function of distance from the disk plane. Right panel: Edges of the wind's blueshifted component vs. the disk's plane. In both panels filled symbols represent data points used in the linear fit to estimate the jet and the wind semi-opening angles and R_{geo} (see Table 2). Best-fits are shown with dashed lines. Data points near the disk plane are not included in the fit due to inadequate sampling of the FWHM and scattering (see Sect. 4 for details). For IRAS 043202 we exclude points above 1.2$''$ as they clearly deviate from a wind-like morphology. HH 30 has the narrowest jet and wind in our sample.

3 Discussion and Conclusions

Different types of disk winds, with distinct kinematic and morphological features, have been discussed in the literature (Sect. 1). X-winds have been invoked to spin down

the accreting star [e.g., 7], while photoevaporative winds might drive disk dispersal [e.g., 8]. Only radially extended MHD winds could solve the longstanding puzzle of how protoplanetary disks accrete [e.g., 2, 16, for recent reviews].

The edge-on orientation of our systems provides a unique advantage to map out the structure of disk winds, with the bright flux of the central star effectively masked by the disk. With NIRSpec IFU spectral imaging, the **respective morphology of** atomic and molecular disk wind components is revealed in striking detail in multiple **Class II** systems for the first time, **on spatial scales reaching down to 30 au from the disk plane**. In all cases, a collimated jet traced by [Fe II] is encased within the wider-angle emission from H_2, and in one case, also CO (v=1-0). The near-infrared molecular emission extends well above 100 au from the disk plane with a characteristic conical shape previously noted in a few other systems [e.g., 17–19]. The **consistent** detection of a pronounced central cavity, marked by a notable absence of emission at the H_2 axial position, is a novel important finding. Moreover, the molecular wind emission appears to be anchored at radial distances < 15 au, well inside the disk radii. High-resolution ground-based spectroscopy of Class I and II sources finds low-velocity H_2 2.12 μm flows reaching **blue-shifted** speeds up to ~ 20 km/s [e.g., 15]. Although H_2 velocities are not measured in our edge-on sources (Sect. 2), similarly low velocities likely characterize the molecular structures we are imaging.

In the case of HH 30, we can also compare the brightest component of the wind traced with NIRSpec in H_2 **and CO (v=1-0)** with the one probed with ALMA in the CO **(J=2-1)** line, as shown in **the left panel of** Figure 4. The CO millimeter emission traces gas flowing at ~ 10 km/s and has a hollow cone shape, but with semi-opening angle $\sim 35°$ [22], considerably wider than **the** $\sim 13°$ **and** $\sim 18°$ semi-opening angles of the warmer H_2 and CO (v=1-0) cones (Table 2 **and caption of Figure 4**). The latter nestle inside the millimeter cavity and, as expected, the average $R_{\rm geo}$ derived from H_2 ($\sim 6 \pm 2$ au) falls below the ~ 10 au deduced from the CO (J=2-1) emission [22]. **These distinctive nested hollow structures might be less discernible at lower disk inclinations. However, observations at lower inclinations provide complementary information, especially on flow velocity, when performed with high-resolution spectroscopy.**

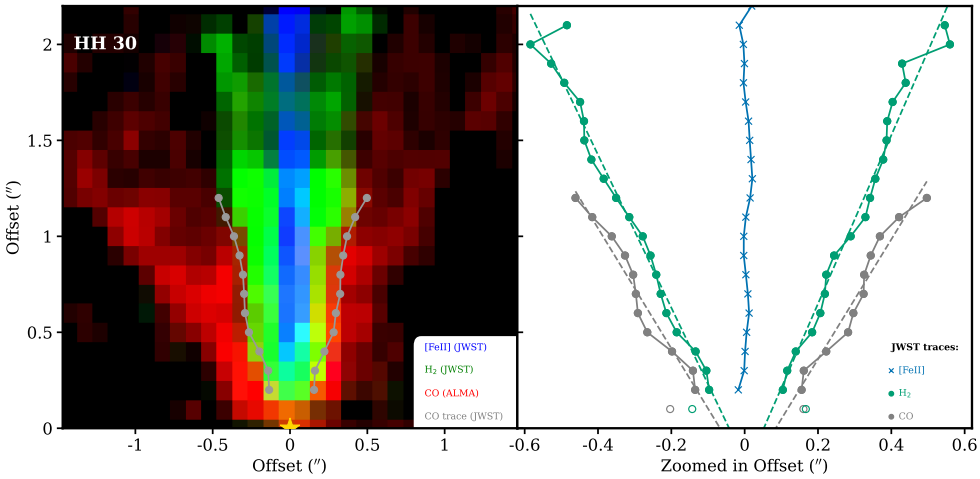

Fig. 4 Left panel: Composite image of HH 30: [Fe II] emission at 1.644 μm (blue) – H_2 emission at 4.695 μm (green) – ALMA CO (2-1) in the LSR velocity 8.3 ± 0.3 km/s (red) and after removing the disk emission [22]. The NIRSpec CO (v=1-0) trace of the outer edge is shown in gray. Right panel: Trace of the [Fe II] jet centroid (blue) and traces of the outer edges of the H_2 (green) and CO (v=1-0, gray) components detected with NIRSpec. The CO (v=1-0) semi-opening angle and geometric radius are $17.8° \pm 2.5°$ and $0.075'' \pm 0.025''$ (10.5 ± 3.5 au) respectively, larger than those measured in H_2 ($13.5° \pm 1.1°$ and $0.045'' \pm 0.01''$ see also Table 2). With the NIRSpec H_2 outer edge inside that of the CO (v=1-0) and both emissions enclosed within the cooler ALMA CO wind, this figure demonstrates the nested structure of disk winds.

Three of our systems appear to have dispersed most of their primordial envelopes **(Sect. 2)**, as indicated by the similarity of single-dish continuum millimeter fluxes and ALMA disk fluxes. The absence of an envelope disfavours the scenario where the observed wide-angle lower-velocity molecular flows would trace infalling envelope material swept-up and entrained by an X-wind **or the jet itself** [44, 45]. Additionally, our $R_{\rm geo}$ are more than an order of magnitude smaller than the disk radii which are the base of the X-wind swept-up shell [46]. The alternative of lower-velocity material entrained at the disk surface by a wide-angle X-wind [11] can be also excluded given the vertical extent **and semi-opening angle** $\leq 50°$ of the H_2 emission detected with NIRSpec. Thus, while jet production by the X-wind cannot be ruled out, its role in generating the observed molecular flows seems very unlikely.

Photoevaporative winds produce molecular flows only beyond several au with velocities of just a few km/s and opening angles around 45° [e.g., 47]. Photoevaporative winds struggle to account for H_2 flows exceeding 5 km/s and cannot match the 100 au vertical extent seen in our NIRSpec data [see 48, for the predicted H_2 2.12 μm emitting region]. Moreover, the near-infrared H_2 and CO cones observed in HH 30 are too narrow (Figure 4) **than those predicted by photoevaporative winds** and the mass flux derived from CO ALMA data exceeds typical photoevaporative mass loss rates [13, 22, 48]. Importantly, photoevaporative winds do not recollimate to produce fast axial jets, hence they would need to be coupled with an MHD wind to reproduce

the narrow [Fe II] emission seen in our sample. These inner winds might shield high-energy photons from the central star, diminishing their capacity to reach the outer disk and drive photoevaporative flows [Figure 8 in 16]. The absence of [Ne II] 12.8 μm low-velocity flows from stars with accretion rates $\gtrsim 10^{-8}\,M_\odot$/yr, akin to those of our sources (Sect. 2), coupled with low-velocity [O I] tracing an inner wind, strongly suggests such shielding [see Section 4.2 in 16].

Among the proposed wind models, radially extended MHD winds are the only ones that **are consistent with** the wind morphologies and nested structures **observed in our sample**. While the initial opening angles at the launch radii are $\geq 30°$, the toroidal component of the magnetic field produces a gradual recollimation [e.g., 43] – field lines close to the co-rotation radius contribute to a fast axial jet, while those further out can explain a range of flow opening angles depending on the scale probed by the observations. With temperature, ionization, and radiation field decreasing as the launch radius increases, a nested velocity structure and morphology are expected [e.g., 6]. H_2 and CO can survive in these winds and trace photoprocesses like those in photodissociation regions and/or internal shocks [e.g., 9]. The one-sided winds of FS Tau B and HH 30 also align with global MHD simulations that account for the non-ideal Hall effect [e.g., 49]**, though differences in the ambient medium, more pronounced in embedded sources, might also contribute to the asymmetry [e.g., 37].**

The rich spectral information in this NIRSpec dataset, with numerous lines of [Fe II] , H_2, and CO (Figure 1), enables physical conditions in the wind components to be determined, including mass loss rates (Bajaj et al. in prep., Beck et al. in prep). Together, the imaging and spectroscopy will clarify whether disk winds are indeed sufficient to drive disk accretion. The implications of wind-driven accretion extend far beyond clarifying how disks accrete. Wind-driven accretion profoundly impacts disk dynamics and planet formation: it slows down the inward drift of solids, thus helping to overcome the radial drift barrier that hinders planet formation [e.g., 4]; and it alters the migration of planetary embryos which enhances the survival of close-in super-Earths [e.g., 5]. Additionally, MHD winds could transport high-temperature materials from the inner Solar System to the comet-forming region [e.g., 50]. These effects could reshape our understanding of how planetary systems form and evolve.

4 Methods

Observations and Data Reduction. Our sources were observed in September 2022 with the JWST NIRSpec IFU instrument as part of our Cycle 1 General Observer program (PI Pascucci, ID 1621). We adopted a 4-point dither pattern to improve the sampling of the PSF, one integration with 30 groups per dither, and integrated for a total on-source time of 30 min per grating. We selected all three high-resolution gratings to cover the entire wavelength range from $\sim 0.98 - 5.2\,\mu$m.

To reduce the data we utilized the JWST calibration pipeline [51] version **'1.13.4.dev19+gbddb39c6'**, which was made available on **January 25, 2024**. The initial stage, `Detector1Pipeline`, implements detector-level corrections on a group-by-group basis. We customized the `jump` step within this stage to detect 'snowballs' in the data and flagged groups after jump with DN above 1000 and any groups within the first 50 seconds. Subsequently, the `Spec2Pipeline` was executed with default parameters **and 'NSClean' on**: this step includes photometric calibration, flat field correction, and World Coordinate System assignment. Because of issues with the default outlier detection and rejection step within the `Spec3Pipeline` stage, we ran a custom script to flag very large positive and negative pixels (J. Morrison, personal communication, 2023). Following this, we ran the `Spec3Pipeline` with the modified 'cal' files and created the image cubes with and without the 'ifualign' mode, the latter avoids any further interpolation and is the preferred product for the analysis carried out in this paper. We inspected the cubes to verify that none of the scientific data were erroneously flagged. Finally, to properly compare NIRSpec IFU data across the full wavelength range in the dataset, the measured data cubes were deconvolved at each wavelength using a corresponding model PSF. **The deconvolution was carried out using the iterative Bayesian-based Richardson-Lucy method [52, 53]. This robust method for sharpening an image has been shown to be both flux conserving and does not result in negative artifacts. Iterations were optimized and visually inspected to ensure that resolutions were matched across the wavelength range of the datasets. Best results were obtained using 12 iterations. The deconvolution was carried out using the python `scikit`-image restoration tools. Post-deconvolution, we confirmed flux conservation by comparing the flux of lines analyzed in this work before and after deconvolution. We also verified that no artifacts were introduced by inspecting continuum-subtracted line maps (see next for their generation) and confirmed that the emission features sharpened to the same resolution level, with PSF broadening as a function of wavelength effectively removed.**

The model PSF datacubes for the NIRSpec IFU mode were generated by deconvolving the corresponding commissioning observations of a point source (PID 1128) by the model NIRSpec data cube. **The latter was** generated using the python based WebbPSF package [54] with the optical path differential (OPD) file that was appropriate for the date of the commissioning observation. In doing this, we constructed a convolution kernel datacube that takes into account optical differences between the empirical data and PSF model calculations. This kernel can hence be used to match any WebbPSF OPD calculation to an observed NIRSpec IFU dataset (Beck et al. in prep). The PSF model used for this dataset study was constructed by

using the WebbPSF OPD model for the time of the observations of HH 30 (26 Sep 2022; with NIRSpec wavefront error of 75nm rms), and convolving by our kernel to match the science data presented here.

Continuum-Subtracted Line Maps. First, we generated total spectra summing up the flux over the entire NIRSpec IFU. These spectra are shown in Figure 1 where, in addition to some of the strongest features and emission lines of interest, we also mark the NIRSpec detectors' gaps with semi-trasparent colors. We note that by plotting the minimum and maximum wavelengths cutoff of the IFU slices, we have taken the most conservative approach. The wavelength range where flux is lost depends on the set of slices where the source flux extends. Hence, some flux is recovered in the semi-transparent regions especially for compact sources like FS Tau B.

To create line-only maps for the [Fe II] and H_2 lines, we adopted the method outlined by [55]. First, **we used the total spectra and** `scipy.optimize.curve_fit` **to fit** a Gaussian profile on top of the continuum **and** determine the total flux (reported in Table 2) and the average line centroid and FWHM. **Monte Carlo simulations show that the line flux uncertainty due to the standard deviation in the nearby continuum is at most a few percent, lower than the 10% absolute flux calibration uncertainty of NIRSpec [24].** Next, we extract the flux at each spaxel and fit a Gaussian+continuum. **We consider a line to be detected if the peak value of the Gaussian profile is at least three times the standard deviation of the continuum, and if the standard deviation around the fitted line decreases after subtracting the best-fit Gaussian+continuum.** Where a line is detected, we calculate the area of the Gaussian for the line-only map and store the centroid to determine which portion of the jet/wind is blueshifted. Where no line is detected, we re-fit only the continuum and set a three-sigma upper limit for the line-only map using the standard deviation of the continuum-subtracted data and the average FWHM. The continuum-only map is derived by averaging the continuum across the line centroid±FWHM. Although not shown here, we have also generated line-only maps for the H_2 2.12 μm and 5.05 μm transitions **with integrated fluxes in Extended Data Table 1.** Their morphologies are the same as that of the **H_2** 0-0 S(9) line which we focus on here because it suffers less than the 2.12 μm from scattering close to the disk plane and it is brighter than the 5.05 μm line.

To construct the continuum-subtracted CO (v=1-0) map, we expand the method above by fitting, at each spaxel, multiple Gaussian profiles across various wavelength segments, all sharing a common continuum. We utilize the ^{12}CO and ^{13}CO line list from the HITRAN database [56], supplemented by additional lines within the CO (v=1-0) fundamental band[1]. The line-only map is generated by summing the areas of all detected ^{12}CO lines. In spaxels where lines are not detected, we provide a three-sigma upper limit, calculated using the standard deviation of the data after continuum subtraction and the average ^{12}CO FWHM from fitting lines in the total NIRSpec IFU spectrum.

[1] http://hebergement.u-psud.fr/edartois/jwst_line_list.html

Jet and Wind Morphologies. To measure the jet position angle (PA), we use the continuum-subtracted [Fe II] 1.644 μm map generated with the default rotation in the STScI pipeline script so that North is pointing up along the y axis. For each pixel along the x-axis, we extract the corresponding y-array, smooth it, and find its peak value (y-peak). We then perform a linear fit of the x values and the identified y-peaks using the `sklearn RANSACRegressor`. The jet PA is the angle between this best-fit line and the direction of North. We repeat the extraction, peak identification, and linear fit across different sets of (x,y) points that exhibit jet emission. Next, we analyze the distribution of the jet PAs and compute the mode, the most frequently occurring PA, and the standard deviation. These are the values reported in Table 2. Note that in all cases the jet PA is perpendicular to the disk PA within the quoted uncertainties.

We determine the blueshited side of the jet from the Gaussian line centroid map which is constructed as discussed in the previous subsection. We then rotate all line-only and continuum maps to an angle that aligns the blueshifted component of the jet with the upper part of the y-axis on the panel. The jet's emission pinpoints the star's position along the x-axis. However, locating the star on the y-axis is more challenging due to the systems being observed close to edge-on. This orientation results in the circumstellar disk obscuring partially or completely the star's emission. For HH 30, IRAS 04302, and Tau 042021, which have a disk inclined by more than 80°, the continuum map traces the flared disk surface, with no emission near the disk plane. For these cases, we extract a profile along the jet emission and identify the midpoint of the non-emissive, or "dark", continuum valley. This midpoint is assigned as the star's y-axis location as well as the disk plane. In FS Tau B, with the disk inclined at $\sim 70°$, the continuum emission appears point-like (see Figure 2) and is likely to trace scattered light in proximity to the central star. We assign the star's y-axis position to **the pixel just below** the peak of the continuum emission.

We use the graduate broadening of the jet emission away from the disk plane to estimate the jet semi-opening angles (θ_j) reported in Table 2. First, we perform horizontal cuts across the [Fe II] rotated line-only images, fit a Gaussian profile, and measure its FWHM. Next, we assess potential artificial broadening of the jet's FWHM due to scattering near the disk plane, along with any insufficient FWHM sampling. For FS Tau B, IRAS 04302, and Tau 042021, we noted that the peak of the jet emission is spread over two columns. Consequently, any FWHM measurement below 1.7 pixels (equivalent to 0.17″) is considered to be undersampled. This is evidenced by the near-constant jet FWHM for FS Tau B and Tau 042021 at distances below 0.5″ from the disk plane, as shown in Figure 3. Hence, we have excluded any data points with FWHM$<$ 0.17″ when determining the jets' semi-opening angles. In contrast, the peak jet emission in HH 30 is more narrowly confined along a single column, which mitigates the sampling issue. For this source, we further compared our FWHM vs distance with that obtained from higher resolution STIS spectral images of the [S II] 6731 Å and [O I] 6300 Å lines [40] and determined that the [Fe II] jet becomes resolvable at distances greater than 1″ from the disk plane. Only these resolvable points were used in our analysis. An Ordinary Least Squares fitting was then applied to the data points unaffected by scattering or poor sampling, which are represented by filled circles in Figure 3. The jet semi-opening angle (θ_j) is calculated from the slope of

the best fit relation, this value along with its uncertainty are provided in Table 2. For FS Tau B and HH 30, where jet semi-opening angles have previously been reported in the literature [40, 57], our values align with the published ones, falling within the estimated uncertainties.

The wind semi-opening angles (θ_w) and geometric radii (R_{geo}) reported in Table 2 are measured on the rotated H_2 0-0 S(9) line-only image. To trace the wind's outer contours, we developed two approaches. The first one follows [58] and relies on calculating the second-order derivative of horizontal cuts across the wind emission and finding its zero values – these values indicate the inflection points that define the wind's edge. However, for complex patchy emission like that displayed by IRAS 04302 the method finds too many inflection points that need to be sorted out manually. As such, we developed a more robust aproach that relieas on fitting Gaussian profiles, typically two but see below, to the same horizontal cuts. We have verified on HH 30 that the wind's edges from the first method are equivalent to the Gaussian centroids plus or minus, depending on the wind's location with respect to the central axis, **half of its** FWHM. For FS TauB and HH30 one Gaussian$\pm$**0.5**$\times$**FWHM** is used when approaching the disk plane. The Gaussian fitting method is applied to all sources and used to determine the wind's properties. Extended Data Figure 1 demonstrates this technique on HH 30. To evaluate if the wind's shape exhibits symmetry around the central axis, we analyze the edges on either side separately. We fit the edges vs. the distance from the star using an Ordinary Least Squares fitting routine. The semi-opening angles (θ_w) of the wind are then calculated as the angles between the best-fit lines and the vertical y-axis. The geometric radii (R_{geo}) are determined by the intersection points of these best-fit lines with the disk's plane, marked by the star's location on the y-axis. Uncertainties for θ_w and R_{geo} are also calculated and reported in Table 2 **and for the CO (v=1-0) in HH 30 in the caption of Fig. 4**.

Data Availability. The JWST data used in this paper can be found at the Mikulski archive for Space Telescope under programs ID 1621 and 1128. The first program covers the four edge-on disks while the second has commissioning data to generate the NIRSpec PSF. Both raw data and fully processed pipeline data can be downloaded from the archive. The spectra integrated over the NIRSpec IFU **(Figure 1) as well as the line-only and continuum maps (Figure 2)** are available through figshare (DOI: 10.6084/m9.figshare.25396258).

Code Availability. The data were reduced with the JWST calibration pipeline version 1.11.2. Upon request, the first author will provide the python scripts to analyze the data and generate figures.

Correspondence and requests for materials should be addressed to I. Pascucci.

Acknowledgments. This work is based on observations made with the NASA/ESA/CSA James Webb Space Telescope. The data were obtained from the Mikulski Archive for Space Telescopes at the Space Telescope Science Institute, which is operated by the Association of Universities for Research in Astronomy, Inc., under NASA

contract NAS 5-03127 for JWST. These observations are associated with the GO Cycle 1 program 1621. I.P. and N.B. acknowledge partial support from NASA/STScI GO grant JWST-GO-01621.001. D. S. acknowledges support from the European Research Council under the Horizon 2020 Framework Program via the ERC Advanced Grant Origins 83 24 28 (PI: Th. Henning). G.D. acknowledges support from the European Research Council (ERC) under the European Union's Horizon Europe research and innovation program (grant agreement No. 101053020, project Dust2Planets, PI F.Ménard). M.V. acknowledges the support from the European Research Council (ERC) under the European Union's Horizon Europe Research & Innovation Programme under grant agreement no. 101039651 (DiscEvol). I.P. thanks D. Deng and F. Long for an initial exploration of the ALMA data for our sources. We acknowledge the use of the following packages: api, astropy, numpy, scipy, sklearn, matplotlib, and pandas.

Author contributions. I.P. led the proposal, carried out the analysis, and wrote the manuscript. N.S. used the JWST pipeline to perform the data reduction. T.B. assisted in the planning of the observations, data reduction, and PSF-deconvolved the reduced datacubes. F.L. provided the ALMA CO (2-1) data for HH 30 and B.S. contributed to the initial script to generate the CO (v=1-0) map and the RGB figures. S.C., S.E., J.N., and U.G. significantly contributed to the interpretation of the results. All authors participated in the discussion of the results and/or commented on the manuscript.

References

[1] Balbus, S.A., Hawley, J.F.: A Powerful Local Shear Instability in Weakly Magnetized Disks. I. Linear Analysis. Astrophys. J. **376**, 214 (1991) https://doi.org/10.1086/170270

[2] Lesur, G., Flock, M., Ercolano, B., Lin, M., Yang, C., Barranco, J.A., Benitez-Llambay, P., Goodman, J., Johansen, A., Klahr, H., Laibe, G., Lyra, W., Marcus, P.S., Nelson, R.P., Squire, J., Simon, J.B., Turner, N.J., Umurhan, O.M., Youdin, A.N.: Hydro-, Magnetohydro-, and Dust-Gas Dynamics of Protoplanetary Disks. In: Inutsuka, S., Aikawa, Y., Muto, T., Tomida, K., Tamura, M. (eds.) Astronomical Society of the Pacific Conference Series. Astronomical Society of the Pacific Conference Series, vol. 534, p. 465 (2023)

[3] Suzuki, T.K., Ogihara, M., Morbidelli, A., Crida, A., Guillot, T.: Evolution of protoplanetary discs with magnetically driven disc winds. Astron. Astrophys. **596**, 74 (2016) https://doi.org/10.1051/0004-6361/201628955 arXiv:1609.00437 [astro-ph.EP]

[4] Taki, T., Kuwabara, K., Kobayashi, H., Suzuki, T.K.: New Growth Mechanism of Dust Grains in Protoplanetary Disks with Magnetically Driven Disk Winds. Astrophys. J. **909**(1), 75 (2021) https://doi.org/10.3847/1538-4357/abd79f arXiv:2004.08839 [astro-ph.EP]

[5] Kimmig, C.N., Dullemond, C.P., Kley, W.: Effect of wind-driven accretion on planetary migration. Astron. Astrophys. **633**, 4 (2020) https://doi.org/10.1051/0004-6361/201936412 arXiv:1910.12889 [astro-ph.EP]

[6] Wang, L., Bai, X.-N., Goodman, J.: Global Simulations of Protoplanetary Disk Outflows with Coupled Non-ideal Magnetohydrodynamics and Consistent Thermochemistry. Astrophys. J. **874**(1), 90 (2019) https://doi.org/10.3847/1538-4357/ab06fd arXiv:1810.12330 [astro-ph.EP]

[7] Shu, F., Najita, J., Ostriker, E., Wilkin, F., Ruden, S., Lizano, S.: Magnetocentrifugally Driven Flows from Young Stars and Disks. I. A Generalized Model. Astrophys. J. **429**, 781 (1994) https://doi.org/10.1086/174363

[8] Alexander, R., Pascucci, I., Andrews, S., Armitage, P., Cieza, L.: The Dispersal of Protoplanetary Disks. In: Beuther, H., Klessen, R.S., Dullemond, C.P., Henning, T. (eds.) Protostars and Planets VI, pp. 475–496 (2014). https://doi.org/10.2458/azu_uapress_9780816531240-ch021

[9] Panoglou, D., Cabrit, S., Pineau Des Forêts, G., Garcia, P.J.V., Ferreira, J., Casse, F.: Molecule survival in magnetized protostellar disk winds. I. Chemical model and first results. Astron. Astrophys. **538**, 2 (2012) https://doi.org/10.1051/0004-6361/200912861 arXiv:1112.3248 [astro-ph.SR]

[10] Shu, F.H., Najita, J., Ostriker, E.C., Shang, H.: Magnetocentrifugally Driven Flows from Young Stars and Disks. V. Asymptotic Collimation into Jets. Astrophys. J. Lett. **455**, 155 (1995) https://doi.org/10.1086/309838

[11] Matsuyama, I., Johnstone, D., Hollenbach, D.: Dispersal of Protoplanetary Disks by Central Wind Stripping. Astrophys. J. **700**(1), 10–19 (2009) https://doi.org/10.1088/0004-637X/700/1/10 arXiv:0904.3363 [astro-ph.EP]

[12] Cunningham, A., Frank, A., Hartmann, L.: Wide-Angle Wind-driven Bipolar Outflows: High-Resolution Models with Application to Source I of the Becklin-Neugebauer/Kleinmann-Low OMC-I Region. Astrophys. J. **631**(2), 1010–1021 (2005) https://doi.org/10.1086/432658 arXiv:astro-ph/0506159 [astro-ph]

[13] Wang, L., Goodman, J.: Hydrodynamic Photoevaporation of Protoplanetary Disks with Consistent Thermochemistry. Astrophys. J. **847**(1), 11 (2017) https://doi.org/10.3847/1538-4357/aa8726 arXiv:1706.03155 [astro-ph.EP]

[14] Evans, I. Neal J., Dunham, M.M., Jørgensen, J.K., Enoch, M.L., Merín, B., van Dishoeck, E.F., Alcalá, J.M., Myers, P.C., Stapelfeldt, K.R., Huard, T.L., Allen, L.E., Harvey, P.M., van Kempen, T., Blake, G.A., Koerner, D.W., Mundy, L.G., Padgett, D.L., Sargent, A.I.: The Spitzer c2d Legacy Results: Star-Formation Rates and Efficiencies; Evolution and Lifetimes. Astrophys. J. Suppl. Ser. **181**(2), 321–350 (2009) https://doi.org/10.1088/0067-0049/181/2/321 arXiv:0811.1059 [astro-ph]

[15] Gangi, M., Nisini, B., Antoniucci, S., Giannini, T., Biazzo, K., Alcalá, J.M., Frasca, A., Munari, U., Arkharov, A.A., Harutyunyan, A., Manara, C.F., Rigliaco, E., Vitali, F.: GIARPS High-resolution Observations of T Tauri stars (GHOsT). II. Connecting atomic and molecular winds in protoplanetary disks. Astron. Astrophys. **643**, 32 (2020) https://doi.org/10.1051/0004-6361/202038534 arXiv:2008.01977 [astro-ph.SR]

[16] Pascucci, I., Cabrit, S., Edwards, S., Gorti, U., Gressel, O., Suzuki, T.K.: The Role of Disk Winds in the Evolution and Dispersal of Protoplanetary Disks. In: Inutsuka, S., Aikawa, Y., Muto, T., Tomida, K., Tamura, M. (eds.) Protostars and Planets VII. Astronomical Society of the Pacific Conference Series, vol. 534, p. 567 (2023). https://doi.org/10.48550/arXiv.2203.10068

[17] Agra-Amboage, V., Cabrit, S., Dougados, C., Kristensen, L.E., Ibgui, L., Reunanen, J.: Origin of the wide-angle hot H_2 in DG Tauri. New insight from SINFONI spectro-imaging. Astron. Astrophys. **564**, 11 (2014) https://doi.org/10.1051/0004-6361/201220488 arXiv:1402.1160 [astro-ph.SR]

[18] Beck, T.L., Bary, J.S.: A Search for Spatially Resolved Infrared Rovibrational Molecular Hydrogen Emission from the Disks of Young Stars. Astrophys. J. **884**(2), 159 (2019) https://doi.org/10.3847/1538-4357/ab4259 arXiv:1909.04730 [astro-ph.SR]

[19] Arulanantham, N., McClure, M.K., Pontoppidan, K., Beck, T.L., Sturm, J.A., Harsono, D., Boogert, A.C.A., Cordiner, M., Dartois, E., Drozdovskaya, M.N., Espaillat, C., Melnick, G.J., Noble, J.A., Palumbo, M.E., Pendleton, Y.J., Terada, H., van Dishoeck, E.F.: JWST MIRI MRS Images of Disk Winds, Water, and CO in an Edge-on Protoplanetary Disk. Astrophys. J. Lett. **965**(1), 13 (2024) https://doi.org/10.3847/2041-8213/ad35c9 arXiv:2402.12256 [astro-ph.SR]

[20] Simon, M., Guilloteau, S., Beck, T.L., Chapillon, E., Di Folco, E., Dutrey, A., Feiden, G.A., Grosso, N., Piétu, V., Prato, L., Schaefer, G.H.: Masses and Implications for Ages of Low-mass Pre-main-sequence Stars in Taurus and Ophiuchus. Astrophys. J. **884**(1), 42 (2019) https://doi.org/10.3847/1538-4357/ab3e3b arXiv:1908.10952 [astro-ph.SR]

[21] Villenave, M., Ménard, F., Dent, W.R.F., Duchêne, G., Stapelfeldt, K.R., Benisty, M., Boehler, Y., van der Plas, G., Pinte, C., Telkamp, Z., Wolff, S., Flores, C., Lesur, G., Louvet, F., Riols, A., Dougados, C., Williams, H., Padgett, D.: Observations of edge-on protoplanetary disks with ALMA. I. Results from continuum data. Astron. Astrophys. **642**, 164 (2020) https://doi.org/10.1051/0004-6361/202038087 arXiv:2008.06518 [astro-ph.SR]

[22] Louvet, F., Dougados, C., Cabrit, S., Mardones, D., Ménard, F., Tabone, B., Pinte, C., Dent, W.R.F.: The HH30 edge-on T Tauri star. A rotating and precessing monopolar outflow scrutinized by ALMA. Astron. Astrophys. **618**, 120 (2018) https://doi.org/10.1051/0004-6361/201731733 arXiv:1808.03285 [astro-ph.GA]

[23] Duchene, G., Menard, F., Stapelfeldt, K., Villenave, M., Wolff, S.G., Perrin, M.D., Pinte, C., Tazaki, R., Padgett, D.L.: JWST imaging of edge-on protoplanetary disks. I. Fully vertically mixed 10μm grains in the outer regions of a 1000 au disk. arXiv e-prints, 2309–07040 (2023) https://doi.org/10.48550/arXiv.2309.07040 arXiv:2309.07040 [astro-ph.EP]

[24] Böker, T., Beck, T.L., Birkmann, S.M., Giardino, G., Keyes, C., Kumari, N., Muzerolle, J., Rawle, T., Zeidler, P., Abul-Huda, Y., Alves de Oliveira, C., Arribas, S., Bechtold, K., Bhatawdekar, R., Bonaventura, N., Bunker, A.J., Cameron, A.J., Carniani, S., Charlot, S., Curti, M., Espinoza, N., Ferruit, P., Franx, M., Jakobsen, P., Karakla, D., López-Caniego, M., Lützgendorf, N., Maiolino, R., Manjavacas, E., Marston, A.P., Moseley, S.H., Ogle, P., Perna, M., Peña-Guerrero, M., Pirzkal, N., Plesha, R., Proffitt, C.R., Rauscher, B.J., Rix, H.-W., Rodríguez del Pino, B., Rustamkulov, Z., Sabbi, E., Sing, D.K., Sirianni, M., te Plate, M., Úbeda, L., Wahlgren, G.M., Wislowski, E., Wu, R., Willott, C.J.: In-orbit Performance of the Near-infrared Spectrograph NIRSpec on the James Webb Space Telescope. Publ. Astron. Soc. Pac. **135**(1045), 038001 (2023) https://doi.org/10.1088/1538-3873/acb846 arXiv:2301.13766 [astro-ph.IM]

[25] Luhman, K.L.: The Stellar Membership of the Taurus Star-forming Region. Astron. J. **156**(6), 271 (2018) https://doi.org/10.3847/1538-3881/aae831 arXiv:1811.01359 [astro-ph.SR]

[26] Furlan, E., Luhman, K.L., Espaillat, C., D'Alessio, P., Adame, L., Manoj, P., Kim, K.H., Watson, D.M., Forrest, W.J., McClure, M.K., Calvet, N., Sargent, B.A., Green, J.D., Fischer, W.J.: The Spitzer Infrared Spectrograph Survey of T Tauri Stars in Taurus. Astrophys. J. Suppl. Ser. **195**(1), 3 (2011) https://doi.org/10.1088/0067-0049/195/1/3

[27] Crapsi, A., van Dishoeck, E.F., Hogerheijde, M.R., Pontoppidan, K.M., Dullemond, C.P.: Characterizing the nature of embedded young stellar objects through silicate, ice and millimeter observations. Astron. Astrophys. **486**(1), 245–254 (2008) https://doi.org/10.1051/0004-6361:20078589 arXiv:0801.4139 [astro-ph]

[28] Di Francesco, J., Johnstone, D., Kirk, H., MacKenzie, T., Ledwosinska, E.: The SCUBA Legacy Catalogues: Submillimeter-Continuum Objects Detected by SCUBA. Astrophys. J. Suppl. Ser. **175**(1), 277–295 (2008) https://doi.org/10.1086/523645 arXiv:0801.2595 [astro-ph]

[29] Reipurth, B., Chini, R., Krugel, E., Kreysa, E., Sievers, A.: Cold dust around Herbig-Haro energy sources : a1300mu.msurvey. Astron. Astrophys. **273**, 221–238 (1993)

[30] Andrews, S.M., Williams, J.P.: Circumstellar Dust Disks in Taurus-Auriga: The Submillimeter Perspective. Astrophys. J. **631**(2), 1134–1160 (2005) https://doi.org/10.1086/432712 arXiv:astro-ph/0506187 [astro-ph]

[31] Andrews, S.M., Rosenfeld, K.A., Kraus, A.L., Wilner, D.J.: The Mass Dependence between Protoplanetary Disks and their Stellar Hosts. Astrophys. J. **771**(2), 129 (2013) https://doi.org/10.1088/0004-637X/771/2/129 arXiv:1305.5262 [astro-ph.SR]

[32] Takami, M., Chrysostomou, A., Ray, T.P., Davis, C.J., Dent, W.R.F., Bailey, J., Tamura, M., Terada, H., Pyo, T.S.: Subaru IR Echelle Spectroscopy of Herbig-Haro Driving Sources. I. H_2 and [Fe II] Emission. Astrophys. J. **641**(1), 357–372 (2006) https://doi.org/10.1086/500352 arXiv:astro-ph/0512268 [astro-ph]

[33] Bacciotti, F., Eislöffel, J., Ray, T.P.: The physical properties of the HH 30 jet from HST and ground-based data. Astron. Astrophys. **350**, 917–927 (1999)

[34] Nisini, B., Antoniucci, S., Alcalá, J.M., Giannini, T., Manara, C.F., Natta, A., Fedele, D., Biazzo, K.: Connection between jets, winds and accretion in T Tauri stars. The X-shooter view. Astron. Astrophys. **609**, 87 (2018) https://doi.org/10.1051/0004-6361/201730834 arXiv:1710.05587 [astro-ph.SR]

[35] White, R.J., Hillenbrand, L.A.: On the Evolutionary Status of Class I Stars and Herbig-Haro Energy Sources in Taurus-Auriga. Astrophys. J. **616**(2), 998–1032 (2004) https://doi.org/10.1086/425115 arXiv:astro-ph/0408244 [astro-ph]

[36] Davis, C.J., Cervantes, B., Nisini, B., Giannini, T., Takami, M., Whelan, E., Smith, M.D., Ray, T.P., Chrysostomou, A., Pyo, T.S.: VLT integral field spectroscopy of embedded protostars: using near-infrared emission lines as tracers of accretion and outflow. Astron. Astrophys. **528**, 3 (2011) https://doi.org/10.1051/0004-6361/201015897

[37] Nisini, B., Navarro, M.G., Giannini, T., Antoniucci, S., Kavanagh, J. Patrick, Hartigan, P., Bacciotti, F., Caratti o Garatti, A., Noriega-Crespo, A., van Dishoeck, E.F., Whelan, E.T., Arce, H.G., Cabrit, S., Coffey, D., Fedele, D., Eislöffel, J., Palumbo, M.E., Podio, L., Ray, T.P., Schultze, M., Urso, R.G., Alcalá, J.M., Bautista, M.A., Codella, C., Greene, T.P., Manara, C.F.: PROJECT-J: JWST Observations of HH46 IRS and Its Outflow. Overview and First Results. Astrophys. J. **967**(2), 168 (2024) https://doi.org/10.3847/1538-4357/ad3d5a arXiv:2404.06878 [astro-ph.GA]

[38] Jensen, S.K., Brittain, S.D., Banzatti, A., Najita, J.R., Carr, J.S., Kern, J., Kozdon, J., Zrake, J., Fung, J.: Spectroastrometric Survey of Protoplanetary Disks with Inner Dust Cavities. Astron. J. **167**(3), 115 (2024) https://doi.org/10.3847/1538-3881/ad1b5d arXiv:2312.17218 [astro-ph.SR]

[39] Eislöffel, J., Mundt, R.: Imaging and Kinematic Studies of Young Stellar Object Jets in Taurus. Astron. J. **115**(4), 1554–1575 (1998) https://doi.org/10.1086/300282

[40] Hartigan, P., Morse, J.: Collimation, Proper Motions, and Physical Conditions in

the HH 30 Jet from Hubble Space Telescope Slitless Spectroscopy. Astrophys. J. **660**(1), 426–440 (2007) https://doi.org/10.1086/513015 arXiv:astro-ph/0701587 [astro-ph]

[41] Erkal, J., Dougados, C., Coffey, D., Cabrit, S., Bacciotti, F., Garcia-Lopez, R., Fedele, D., Chrysostomou, A.: Launching the asymmetric bipolar jet of DO Tau. Astron. Astrophys. **650**, 46 (2021) https://doi.org/10.1051/0004-6361/202038977 arXiv:2104.07484 [astro-ph.SR]

[42] Arulanantham, N., McClure, M.K., Pontoppidan, K., Beck, T.L., Sturm, J.A., Harsono, D., Boogert, A.C.A., Cordiner, M., Dartois, E., Drozdovskaya, M.N., Espaillat, C., Melnick, G.J., Noble, J.A., Palumbo, M.E., Pendleton, Y.J., Terada, H., van Dishoeck, E.F.: JWST MIRI MRS Images Disk Winds, Water, and CO in an Edge-On Protoplanetary Disk. arXiv e-prints, 2402–12256 (2024) https://doi.org/10.48550/arXiv.2402.12256 arXiv:2402.12256 [astro-ph.SR]

[43] Blandford, R.D., Payne, D.G.: Hydromagnetic flows from accretion disks and the production of radio jets. Mon. Not. R. Astron. Soc. **199**, 883–903 (1982) https://doi.org/10.1093/mnras/199.4.883

[44] Ai, T.-H., Liu, C.-F., Shang, H., Johnstone, D., Krasnopolsky, R.: A Unified Model for Bipolar Outflows from Young Stars: Kinematic and Mixing Structures in HH 30. arXiv e-prints, 2402–02529 (2024) https://doi.org/10.48550/arXiv.2402.02529 arXiv:2402.02529 [astro-ph.SR]

[45] Rabenanahary, M., Cabrit, S., Meliani, Z., Pineau des Forêts, G.: Wide-angle protostellar outflows driven by narrow jets in stratified cores. Astron. Astrophys. **664**, 118 (2022) https://doi.org/10.1051/0004-6361/202243139 arXiv:2204.05850 [astro-ph.SR]

[46] Liang, L., Johnstone, D., Cabrit, S., Kristensen, L.E.: Steady Wind-blown Cavities within Infalling Rotating Envelopes: Application to the Broad Velocity Component in Young Protostars. Astrophys. J. **900**(1), 15 (2020) https://doi.org/10.3847/1538-4357/aba830 arXiv:2007.13744 [astro-ph.SR]

[47] Komaki, A., Nakatani, R., Yoshida, N.: Radiation Hydrodynamics Simulations of Protoplanetary Disks: Stellar Mass Dependence of the Disk Photoevaporation Rate. Astrophys. J. **910**(1), 51 (2021) https://doi.org/10.3847/1538-4357/abe2af arXiv:2012.14852 [astro-ph.EP]

[48] Rab, C., Weber, M., Grassi, T., Ercolano, B., Picogna, G., Caselli, P., Thi, W.-F., Kamp, I., Woitke, P.: Interpreting molecular hydrogen and atomic oxygen line emission of T Tauri disks with photoevaporative disk-wind models. Astron. Astrophys. **668**, 154 (2022) https://doi.org/10.1051/0004-6361/202244362 arXiv:2210.15486 [astro-ph.SR]

[49] Béthune, W., Lesur, G., Ferreira, J.: Global simulations of protoplanetary disks

with net magnetic flux. I. Non-ideal MHD case. Astron. Astrophys. **600**, 75 (2017) https://doi.org/10.1051/0004-6361/201630056 arXiv:1612.00883 [astro-ph.EP]

[50] Giacalone, S., Teitler, S., Königl, A., Krijt, S., Ciesla, F.J.: Dust Transport and Processing in Centrifugally Driven Protoplanetary Disk Winds. Astrophys. J. **882**(1), 33 (2019) https://doi.org/10.3847/1538-4357/ab311a arXiv:1907.04961 [astro-ph.SR]

[51] Bushouse, H., Eisenhamer, J., Dencheva, N., Davies, J., Greenfield, P., Morrison, J., Hodge, P., Simon, B., Grumm, D., Droettboom, M., Slavich, E., Sosey, M., Pauly, T., Miller, T., Jedrzejewski, R., Hack, W., Davis, D., Crawford, S., Law, D., Gordon, K., Regan, M., Cara, M., MacDonald, K., Bradley, L., Shanahan, C., Jamieson, W., Teodoro, M., Williams, T.: JWST Calibration Pipeline. Zenodo (2023). https://doi.org/10.5281/zenodo.8140011

[52] Richardson, W.H.: Bayesian-Based Iterative Method of Image Restoration. Journal of the Optical Society of America (1917-1983) **62**(1), 55 (1972)

[53] Lucy, L.B.: An iterative technique for the rectification of observed distributions. Astron. J. **79**, 745 (1974) https://doi.org/10.1086/111605

[54] Perrin, M.D., Sivaramakrishnan, A., Lajoie, C.-P., Elliott, E., Pueyo, L., Ravindranath, S., Albert, L.: Updated point spread function simulations for JWST with WebbPSF. In: Oschmann, J. Jacobus M., Clampin, M., Fazio, G.G., MacEwen, H.A. (eds.) Space Telescopes and Instrumentation 2014: Optical, Infrared, and Millimeter Wave. Society of Photo-Optical Instrumentation Engineers (SPIE) Conference Series, vol. 9143, p. 91433 (2014). https://doi.org/10.1117/12.2056689

[55] Beck, T.L., McGregor, P.J., Takami, M., Pyo, T.-S.: Spatially Resolved Molecular Hydrogen Emission in the Inner 200 AU Environments of Classical T Tauri Stars. Astrophys. J. **676**(1), 472–489 (2008) https://doi.org/10.1086/527528 arXiv:0711.3844 [astro-ph]

[56] Gordon, I.E., Rothman, L.S., Hargreaves, R.J., Hashemi, R., Karlovets, E.V., Skinner, F.M., Conway, E.K., Hill, C., Kochanov, R.V., Tan, Y., Wcisło, P., Finenko, A.A., Nelson, K., Bernath, P.F., Birk, M., Boudon, V., Campargue, A., Chance, K.V., Coustenis, A., Drouin, B.J., Flaud, J.-M., Gamache, R.R., Hodges, J.T., Jacquemart, D., Mlawer, E.J., Nikitin, A.V., Perevalov, V.I., Rotger, M., Tennyson, J., Toon, G.C., Tran, H., Tyuterev, V.G., Adkins, E.M., Baker, A., Barbe, A., Canè, E., Császár, A.G., Dudaryonok, A., Egorov, O., Fleisher, A.J., Fleurbaey, H., Foltynowicz, A., Furtenbacher, T., Harrison, J.J., Hartmann, J.-M., Horneman, V.-M., Huang, X., Karman, T., Karns, J., Kassi, S., Kleiner, I., Kofman, V., Kwabia-Tchana, F., Lavrentieva, N.N., Lee, T.J., Long, D.A., Lukashevskaya, A.A., Lyulin, O.M., Makhnev, V.Y., Matt, W., Massie, S.T., Melosso, M., Mikhailenko, S.N., Mondelain, D., Müller, H.S.P., Naumenko, O.V., Perrin, A., Polyansky, O.L., Raddaoui, E., Raston, P.L., Reed, Z.D., Rey, M.,

Richard, C., Tóbiás, R., Sadiek, I., Schwenke, D.W., Starikova, E., Sung, K., Tamassia, F., Tashkun, S.A., Vander Auwera, J., Vasilenko, I.A., Vigasin, A.A., Villanueva, G.L., Vispoel, B., Wagner, G., Yachmenev, A., Yurchenko, S.N.: The HITRAN2020 molecular spectroscopic database. J. Quant. Spectrosc. Radiat. Transf. **277**, 107949 (2022) https://doi.org/10.1016/j.jqsrt.2021.107949

[57] Mundt, R., Ray, T.P., Raga, A.C.: Collimation of stellar objects - constraints from the observed spatial structure. II. Observational results. Astron. Astrophys. **252**, 740–761 (1991)

[58] Habel, N.M., Megeath, S.T., Booker, J.J., Fischer, W.J., Kounkel, M., Poteet, C., Furlan, E., Stutz, A., Manoj, P., Tobin, J.J., Nagy, Z., Pokhrel, R., Watson, D.: An HST Survey of Protostellar Outflow Cavities: Does Feedback Clear Envelopes? Astrophys. J. **911**(2), 153 (2021) https://doi.org/10.3847/1538-4357/abded8 arXiv:2102.06717 [astro-ph.GA]

Extended Data

This section includes a table and a figure, specifically Extended Data Table 1 and Extended Data Figure 1.

Extended Data Table 1 Integrated line fluxes for the H_2 2.12 μm and 5.05 μm transitions.

Source	H_2 2.12 μm (erg/s/cm^2)	H_2 5.05 μm (erg/s/cm^2)
FS Tau B	5.0×10^{-15}	3.7×10^{-15}
HH 30	3.2×10^{-15}	9.2×10^{-16}
IRAS 04302	4.1×10^{-15}	1.9×10^{-15}
Tau 042021	9.9×10^{-16}	4.1×10^{-16}

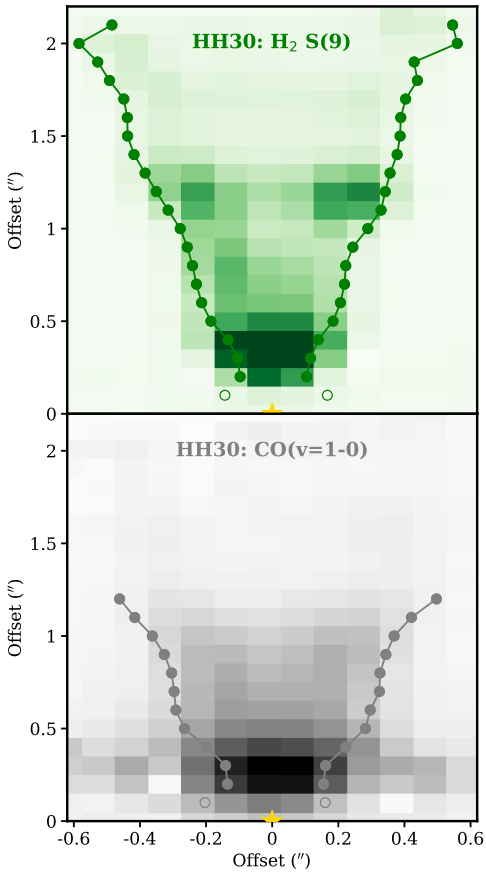

Extended Data Fig. 1 Figure demonstrating our custom edge detection technique applied to HH 30. Upper panel: H_2 0-0 S(9) **map and traces of the outer edge (circles). Lower panel: CO (v=1-0) map and traces of the outer edge (circles).**